geosciences

MDPI

Article

Back-Arc Spreading Centers and Superfast Subduction: The Case of the Northern Lau Basin (SW Pacific Ocean)

Camilla Palmiotto [1,*], Eleonora Ficini [1,2], Maria Filomena Loreto [1], Filippo Muccini [2,3] and Marco Cuffaro [2]

[1] Istituto di Scienze Marine, Consiglio Nazionale delle Ricerche, 40129 Bologna, Italy; eleonora.ficini@bo.ismar.cnr.it (E.F.); filomena.loreto@bo.ismar.cnr.it (M.F.L.)
[2] Istituto di Geologia Ambientale e Geoingegneria, Consiglio Nazionale delle Ricerche, 00185 Roma, Italy; filippo.muccini@ingv.it (F.M.); marco.cuffaro@igag.cnr.it (M.C.)
[3] Istituto Nazionale di Geofisica e Vulcanologia (INGV), 00143 Roma, Italy
* Correspondence: camilla.palmiotto@bo.ismar.cnr.it; Tel.: +39-051-6398900

Abstract: The Lau Basin is a back-arc region formed by the subduction of the Pacific plate below the Australian plate. We studied the regional morphology of the back-arc spreading centers of the Northern Lau basin, and we compared it to their relative spreading rates. We obtained a value of 60.2 mm/year along the Northwest Lau Spreading Centers based on magnetic data, improving on the spreading rate literature data. Furthermore, we carried out numerical models including visco-plastic rheologies and prescribed surface velocities, in an upper plate-fixed reference frame. Although our thermal model points to a high temperature only near the Tonga trench, the model of the second invariant of the strain rate shows active deformation in the mantle from the Tonga trench to ~800 km along the overriding plate. This explains the anomalous magmatic production along all the volcanic centers in the Northern Lau Back-Arc Basin.

Keywords: sea floor spreading; back-arc spreading centers; superfast subduction

Citation: Palmiotto, C.; Ficini, E.; Loreto, M.F.; Muccini, F.; Cuffaro, M. Back-Arc Spreading Centers and Superfast Subduction: The Case of the Northern Lau Basin (SW Pacific Ocean). *Geosciences* **2022**, *12*, 50. https://doi.org/10.3390/geosciences12020050

Academic Editors: Jesus Martinez-Frias and Olivier Lacombe

Received: 13 December 2021
Accepted: 15 January 2022
Published: 20 January 2022

1. Introduction

According to the theory of plate tectonics, most of the oceanic lithosphere originates along the mid-ocean ridges (MORs), where the boundaries between two different plates move apart [1]. New melt rises below the MORs through a process of adiabatic decompression of the mantle, coming into contact with sea water. It cools, solidifies, acquires the magnetization of the Earth's magnetic field, and begins to migrate laterally and symmetrically on both sides of the ridge [2,3].

Seafloor spreading can also occur in back-arc basins (BABs) along convergent plate boundaries [4]. The progressive extension of the overriding plate is connected to the rate and the direction of subduction [5–10]. It creates progressively: (a) the thinning of the crust; (b) the formation of a morphological depression intruded by magmatic bodies; (c) a system of segments of spreading centers in the middle of the basin. Morphology of spreading centers depends mainly on the thermal state and composition of the subridge upwelling mantle, on the magma supply, and on the spreading rate [11–13]; in particular, along back-arc spreading centers (BASCs) it belongs to the geodynamic evolution of each single subduction system [14] and to the structural inheritance from the overriding plate [15].

Examples of back-arc spreading centers are the Mariana in the Pacific Ocean [16–18], the East Scotia Ridge in the Southern Atlantic Ocean [19,20], and the Lau Spreading Centers in the SW Pacific Ocean [4,21,22].

The Lau Basin (Figure 1) is formed by the Pacific-Australian plate convergence at the North of New Zealand [4,21,22]. It started to open ~3.5/4 Ma [23–25], evolving from back-arc rifting to back-arc spreading [26]. The formation of a new oceanic crust occurs South of the Lau Extensional Transform Zone (LETZ), between the Lau and the Tonga

Ridges (Figure 1): a fast system of BASCs propagates southward in the Havre Trough (West of the Kermadec Subduction Zone; Figure 1), considered to be in a rifting stage [4,22,26–29].

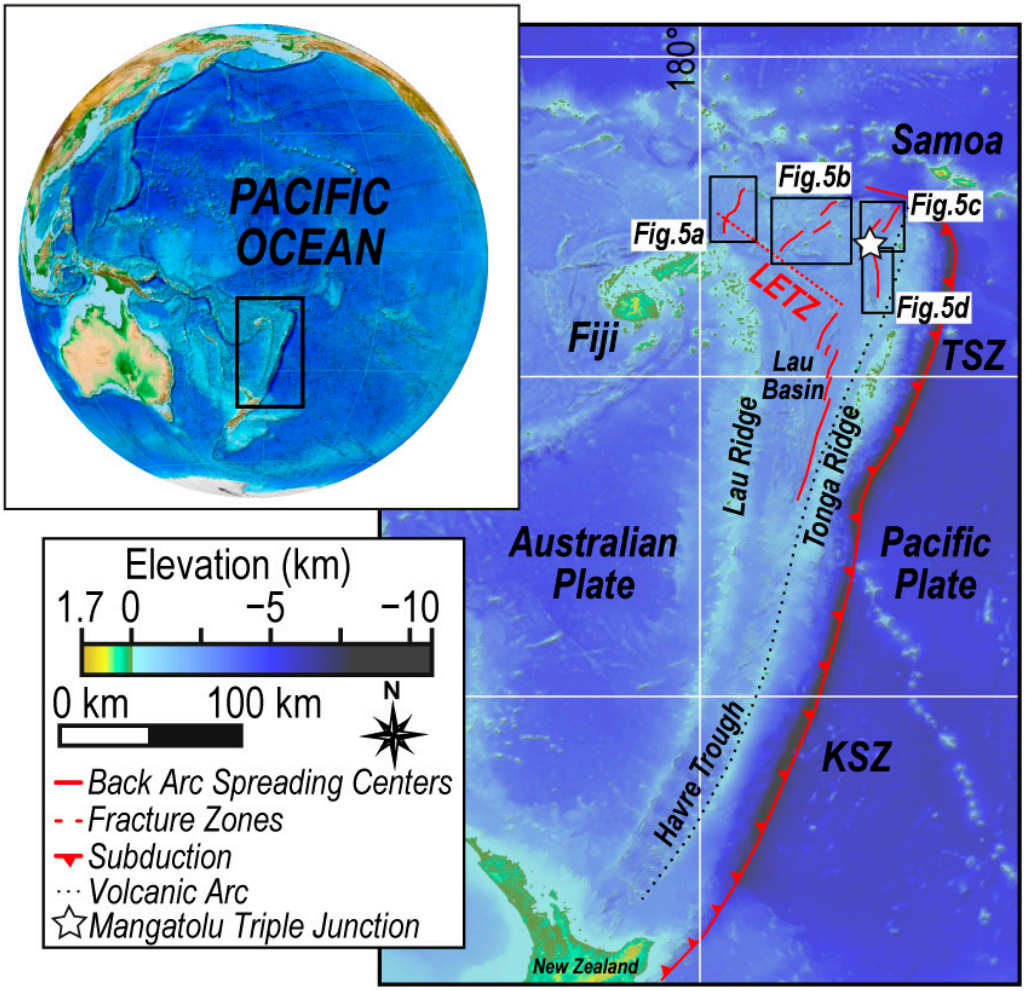

Figure 1. Geographical map of the Lau Basin in the Pacific Ocean. Tectonic features drawn have been digitized from [30]. LETZ: Lau Extensional Transform Zone; TSZ: Tonga Subduction Zone; KSZ: Kermadec Subduction Zone.

Here we focus on the Northern Lau Basin, located between the islands of Fiji and Samoa (Figure 1), extending for about 800 km from the Tonga Subduction Zone (TSZ), the fastest subduction on Earth (~240 mm/year in the Northern part of the TSZ) [31]. This region is a good laboratory to study how the mantle influences magmatic production in the overriding plate along a super-fast subduction. In fact, this region stands out from other oceanic back-arc basins (BABs), because it shows not a single but several parallel and active segments of spreading centers in different points of the basin (Figure 2a): in the Western part, ~760 km from the TSZ, the Futuna Spreading Center (FSC); in the central part, ~500 km from the TSZ, the Northwest Lau Spreading Center (NWLSC) and the North Lau Spreading Center (NLSC); in the Eastern part, ~200 km from the TSZ, the Northeast Lau Spreading Center (NELSC), and the Fonualei Rift and Spreading Center (FRSC).

An intense seismicity characterizes this region, with earthquakes ranging from 0 to >600 km of depth (Figure 2a): shallow earthquakes are distributed all along the basin; intermediate earthquakes only in the eastern basin, ~200 km West of the TSZ, along the NELSC and the FRSC; deep earthquakes only in the central and western part of the region, from the NWLSC and the FSC. Compressive focal mechanisms are located predominantly along the TSZ, indicating the subduction of the Pacific plate below the Australian plate.

Strike-slip focal mechanisms are distributed in the Southern part of the FSC, along the LETZ from the NWLSC to the CLSC (Central Lau Spreading Center), and along the northern region (between FSC and NLSC, and between NLSC and NELSC).

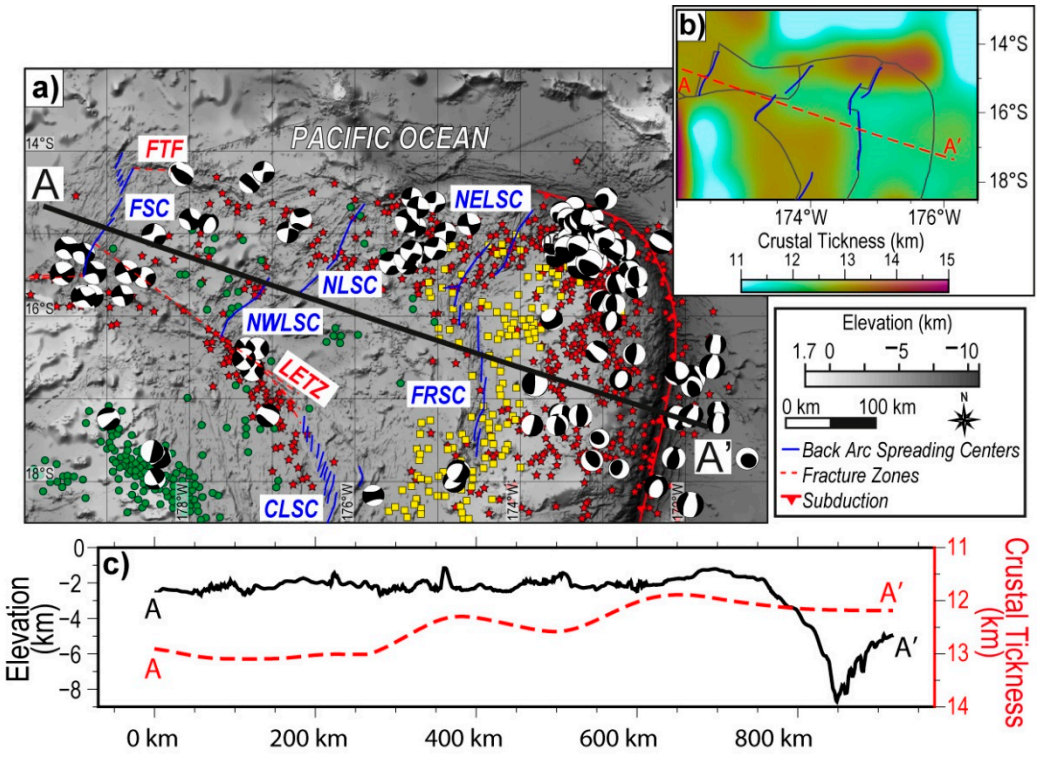

Figure 2. (**a**) Shaded relief image of the Northern Lau Basin and distribution of earthquakes and focal mechanism. Tectonic features drawn have been digitized from [30]. Red stars: earthquakes from 0 to 70 km of depth; yellow squares: earthquakes from 71 to 300 km of depth; green circles: earthquakes >301 km of depth. Distributions of earthquakes and focal mechanisms are from the USGS database archives (http://earthquake.usgs.gov/, accessed on 1 March 2021) and from the CMT catalog [32,33]. Map of seismicity is generated by using the GMT open source [34]: green stars are the earthquake epicenters downloaded from USGS database with Mw > 5 (accessed on 28 May 2021); red stars are the earthquake epicenters downloaded from Harvard CMT Catalog with Mw > 5 recorded from January 1976 to March 2021, of these, those with Mw > 5.6, the focal mechanism were plotted (accessed on 23 March 2021). FSC: Futuna Spreading Center; NWLSC: Northwest Lau Spreading Center; NLSC: North Lau Spreading Center; NELSC: Northeast Lau Spreading Center; FRSC: Fonualei Rift and Spreading Center; CLSC: Central Lau Spreading Center; LETZ: Lau Extensional Transform Zone. (**b**) Global Crust Thickness, e.g., the depth of the Moho from the CRUST1.0 dataset at 1° × 1° resolution, http://igppweb.ucsd.edu/gabi/crust1.html, accessed on 1 June 2021), with location of the profile AA′. The scientific color map used is based on [35]. The black lines are the plate boundaries from [36,37], whereas the blue lines are tectonic features highlighted from this study. (**c**) Bathymetric (solid black line) vs. crustal thickness (dashed red line) profiles show a thinning of the crust toward the Pacific subduction trench.

According to [38], most strike-slip faulting is due to the re-activation of "older" normal faults along spreading centers. Normal focal mechanisms are located along the southern part of the FRSC, where the modern rift is propagating [39].

Global models of the crustal thickness, e.g., the depth of the Moho from the CRUST1.0 dataset at 1° × 1° resolution (http://igppweb.ucsd.edu/gabi/crust1.html, accessed on 1 June 2021), show a depth variation along a selected profile (Figure 2b,c). This profile is NW-SE oriented and it crosses for ~800 km from the TSZ to the Northern Lau Basin. According to our model and to [40], crustal thinning characterizes the first ~200 km from

the TSZ (the Tonga Ridge is 11–13 km thick); low crustal thinning is located also in the central Northern Lau Basin, ~450 km from the TSZ (Figure 2b,c).

Based on bathymetry, magnetization, acoustic imagery, and seismicity data, a first kinematic model for the opening of the Lau BAB during the last 3 Ma was created by [30]; plate kinematic reconstructions of the Tonga–Kermadec subduction have also been achieved by [41,42]. We did a plate reconstruction of our study area during the last 1 Ma using the GPlates software (Figure 3). Plate reconstructions and their related velocities are described relative to a fixed Australia, including relative plate motions and plate polygons provided by [37,43] (and reference therein). In that framework, the Pacific plate moves westward relative to Australia, while the Tonga microplate rotates clockwise, producing extension and back-arc spreading in the Lau Basin, due to the faster convergence of the Pacific during the last 1 Ma (Figure 3).

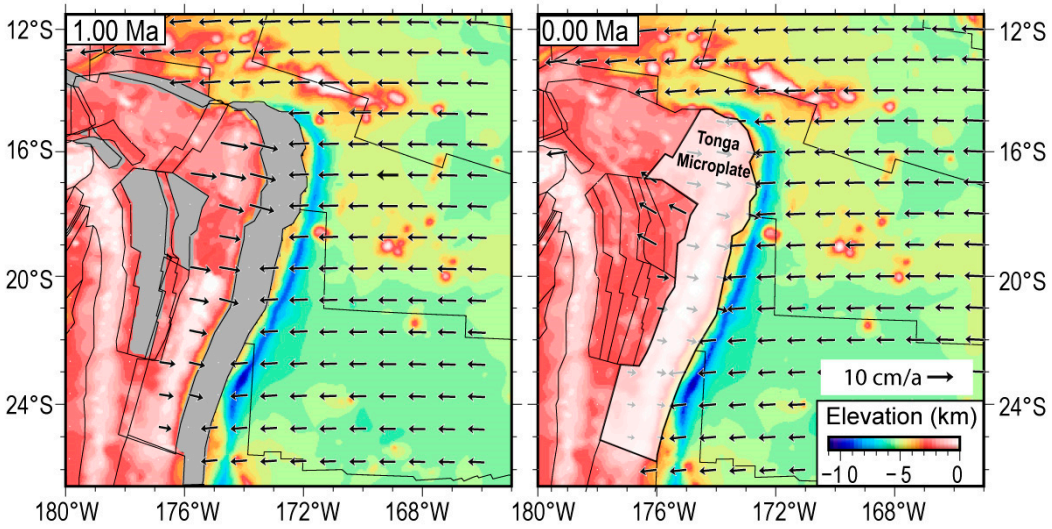

Figure 3. Plate reconstructions of the Northern Lau Basin region for the last 1 Ma. Plate displacements and velocities were computed with respect to the fixed Australia, using the GPlates software (www.gplates.com, accessed on 1 July 2021), also including relative plate motions and plate polygons (black solid lines) obtained by [37]. White polygon in the 0 Ma panel indicates the Tonga microplate. Grey areas at the right and left side of the Tonga microplate in the 1 Ma panel indicate a past and present oceanic crust, respectively.

Concerning the regional morphology, Refs. [44,45] produced a detailed description of the bathymetry of the FSC region with several morphological and tectonic maps. A high-resolution bathymetric map of the NELSC and of the FRSC is shown in [39], where the full spreading rate has been calculated for each ridge segment based on GPS measurements. A bathymetric map of the NWLSC and NLSC (or RR, Rochambeau Rift) are shown in [46]; geological and structural evolution of the NE Lau BAB and of the FRSC has been published by [47].

In this paper we used the GEBCO 2020 bathymetric dataset in order to perform a regional analysis of the morpho-lineaments along all the spreading segments in the Northern Lau Basin; in particular, our main contribution is a regional morphological analysis of the NWLSC and, based on magnetic data, a measure of its full spreading rate. We compared the morphology of the back-arc spreading centers with their relative spreading rates and analyzed the main trend of their morpho-lineaments using rose diagrams. Furthermore, we carried out 2D numerical models including visco-plastic rheologies and prescribed surface velocities, in an upper plate-fixed reference frame.

2. Materials and Methods

2.1. Bathymetry and Morphological Analysis

Regional bathymetry of the Lau Basin was performed using grid data with a 30 arc-seconds resolution downloaded from the GEBCO website (General Bathymetric Chart of the Oceans; GEBCO Compilation Group (2021) GEBCO 2021 Grid; doi:10.5285/c6612cbe-50b3-0cff-e053-6c86abc09f8f). The Global Mapper Software (version 13) has been used to perform the spatial analysis and the regional morpho-structural analysis of the area, and to create 2D digital elevation images. Rose diagrams were created to obtain the trend of morphological and tectonic lineaments, using the open source software GeoRose (http://www.yongtechnology.com/download1/georose/, accessed on 1 April 2021). Our analysis of the morpho-lineaments was based on publications on the morphology of mid-ocean ridges and oceanic fracture zones [11–13,48–55]. Morpho-lineaments have been divided into: (1) fracture zones (i.e., large ocean seafloor topographic irregularities in a seismically active zone and in seismically inactive areas); (2) spreading centers (i.e., mid-oceanic mountain systems of global extent coinciding with the youngest ocean crust); (3) escarpments (i.e., elongated features with linear, steep slopes >5°, separating sectors of the ocean floor); (4) axis of abyssal hills (i.e., crest of isolated and elongated abyssal hills); (5) axis of abyssal valley (i.e., axis of an isolated and elongated abyssal valley); (6) volcanoes (i.e., seamounts with circular shape located along axis and flanks of mid-ocean ridges). The 3D images were created using 3DEM (Visualization Software created by Richard Horne, USGS, http://www.hangsim.com/3dem/, accessed on 01 July 2021). The software Adobe Illustrator (CS2 version) was used to assemble figures and to create the final conceptual models.

2.2. Magnetic Data

We used the WEST06MV magnetic track lines available from the Marine Trackline Geophysical Data [56]. Although this line was acquired back in 1994, the magnetic field was sampled every 400 m on average, which is enough for our purposes. It is commonly accepted that NWLSC was an active spreading segment during the last 1 Ma [16,41], pointing out a fixed constraint in the magnetic modeling. Due to the limited extension of the magnetic line, we focused the magnetic forward modeling to the last 0.78 Ma (Brunhes chrone). We calculated the magnetic anomalies from the line acquired in 1994 by subtracting the IGRF-12 model [57]. The anomaly was used to obtain the medium full spreading rate following the approach proposed by [58] and based on the geomagnetic polarity time scale of [59]. Magnetization intensity of 10 A/m on axis and 5 A/m off axis, respectively, and a constant source layer thickness of 0.5 km, were assumed in the modeling; declination and inclination come from the calculated IGRF model.

2.3. Numerical Model

Very simple supporting numerical computations were done using the ASPECT (Advanced Solver for Problems in the Earth's Convection) code version 2.2.0 [60–62]. It is based on the solution of the conservation of momentum (1), mass (2)—Stokes equations—and coupled energy (3) equation [62,63] using the Finite Elements Method.

$$-\nabla\cdot\left[2\eta\left(\varepsilon(u)-\frac{1}{3}(\nabla\cdot u)1\right)\right]+\nabla p=\rho g, \tag{1}$$

$$\nabla\cdot(\rho u)=0, \tag{2}$$

$$\left(\rho C_p-\rho T\Delta S\frac{\partial X}{\partial T}\right)\left(\frac{\partial T}{\partial t}+u\cdot\nabla T\right)-\nabla\cdot k\nabla T=\rho H \tag{3}$$
$$+2\eta\left(\varepsilon(u)-\frac{1}{3}(\nabla\cdot u)1\right):\left(\varepsilon(u)-\frac{1}{3}(\nabla\cdot u)1\right)$$
$$+\alpha T(u\cdot\nabla p)$$

$$+ \rho T \Delta S \frac{\partial X}{\partial p} u \cdot \nabla p.$$

In the above equations η is the viscosity, $\varepsilon(u) = \frac{1}{2}\left(\nabla u + \nabla u^T\right)$ is the symmetric gradient of velocity, i.e., the strain rate, $u = u(x,t)$ is the velocity field, $p = p(x,t)$ is the pressure field, ρ is the density, T is the temperature, g is the gravity vector, C_p is the specific heat capacity, t is time, ΔS is the change in entropy at a phase transition, together with the derivatives of the phase function $X = X(p, T, c, x)$, where c is the compositional field and x the spatial variable, with respect to temperature and pressure, k is the thermal conductivity, H is the intrinsic specific heat production, and α the linear thermal expansion coefficient. Models carried out in this work use visco-plastic material model implemented in ASPECT, taking into account both plastic and non-linear viscous deformation [64]. Viscous stresses are bounded from the Drucker-Prager yield criterion (4), which in the 2D form is equivalent to the Mohr-Coulomb yield criterion.

$$\sigma_y = Ccos(\phi) + Psin(\phi), \tag{4}$$

where, σ_y is the yield stress, C is the cohesion, ϕ is the angle of internal friction and P is the pressure. If ϕ is 0, the yield stress is fixed and equal to the cohesion (Von Mises yield criterion) [62]. The models were carried out in a 2D rectangular box 2000 km wide and of 660 km depth (Figure 4), with free slip boundary conditions at the top of the numerical domain and prescribed boundary conditions at the right boundary of the numerical domain. At the bottom and left-hand side of the numerical domain, to simulate "open" boundary conditions, we prescribed the lithostatic pressure as a boundary condition for the stress using the "initial lithostatic pressure" plugin; this allowed the material to flow in and out according to the flow induced by the moving plate (Figure 4). Prescribed boundary conditions (i.e., imposed velocity) were applied to the right boundary of the numerical domain (Figure 4), simulating that of [65], according to [66].

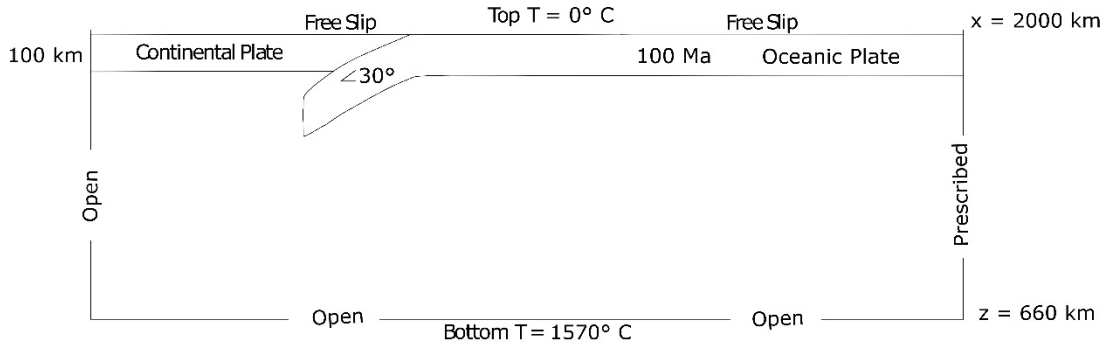

Figure 4. Numerical model setup. Models were carried out in a 2D box 2000 km wide and 660 km deep. The trench is positioned at 500 km with respect to the left boundary of the numerical domain (corresponding to the zero). The upper continental plate has a thickness of 100 km, whereas the lower oceanic plate has an age of 100 Ma. The starting configuration of this model include a partially subducted slab in the mantle at 200 km depth, with a dip of 30°. Free slip boundary conditions were applied to the top of the numerical domain, whereas "open" boundary conditions were simulated at the left and bottom sides using the "initial lithostatic pressure" plugin that allowed the material to flow in and out according to the flow induced by the moving plate. Prescribed boundary conditions were implemented at the right boundary of the numerical domain, simulating that of [65], according to [66].

The velocity applied to the right boundary corresponds to the subduction velocity (V_S), calculated at Lau-Basin as in [66].

V_S is the effective velocity with which a plate enters the mantle. It is in fact the result of $V_H - V_L$ [67], where V_H is the slab hinge (i.e., the point of maximum curvature

on a subducting slab) velocity and V_L the convergence velocity of the subducting plate. All velocity data and references are shown in Table 1. The starting configuration of this model include a slab partially subducted, being within the mantle at 200 km depth, with a dip of 30°. This setup was chosen due to the continental nature of some microplate remnants [37,40,43]. The upper continental plate has a thickness of 100 km, whereas the lower oceanic plate has an age of 100 Ma [68–70]. The model run represents the evolution of the Tonga subduction zone (Lau-Basin) during the last 1 Ma. Rheological and thermal parameters used for the calculation are shown in Table 2.

Table 1. Velocity boundary conditions. In this table, subduction velocity applied to the subducting plate and parameters used to compute it (i.e., $V_S = V_H - V_L$) are shown, together with their references. V_S: subduction velocity; V_H: slab hinge velocity; V_L: convergence velocity.

V_H (mm/year)	Reference for V_H	V_L (mm/year)	Reference for V_L	V_S (mm/year)
131.3	[71]	81.7 ± 0.8	[36]	213.0

Table 2. Rheological and thermal parameters. Here, some thermal and rheological parameters are implemented in the numerical experiments [62,64,72,73].

	Overriding Plate	Subducting Plate	Mantle
Reference density (kg/m^3)	3300	3300	3300
Viscosity prefactors (dislocation creep)	1×10^{-20}	1×10^{-21}	5×10^{-30}
Stress exponents	3.5	3.5	1
Thermal diffusivity (W/m K)	1.3×10^{-6}	1.3×10^{-6}	1.3×10^{-6}
Thermal expansivity (1/K)	2×10^{-5}	2×10^{-5}	2×10^{-5}
Heat capacity (J/kg K)	1250	1250	1250

3. Results

3.1. Morphological and Magnetic Analysis

The FSC is located in the Western part of the Northern Lau Basin, ~760 km from the TSZ (Figures 1 and 5a). The Northern part of the FSC shows a NNE–SSW morphological rise that reaches 1750 m below sea level (Figure 5a). We identified 179 morpho-lineaments in this region, most of them oriented NNE–SSW, located respectively West and East of the axis FSC (Figure 5a).

To the North, the FSC is offset by the Futuna Transform Fault (FTF), a right-slip fault-oriented WNW–ESE. The nodal basin is ~2800 m deep; the inside corner reaches 2000 m below sea level; the outside corner is characterized by curving (J-shaped) ridges. The bathymetry of the FSC changes South of the LETZ: the morphological rise disappears, and the area displays a deep and large valley (~3500 m deep and 40 km wide), with alternating NNE–SSW and/or N–S hills and valleys. Escarpments more than 5° steep have been identified, as well as volcanic seamounts along the flanks of the FSC; no seamounts have been detected in the Southern part.

The NLSC and the NWLSC are located in the central part of the Northern Lau Basin, ~500 km from the TSZ (Figures 1 and 5b). The NWLSC is a NE–SW morphological rise that reaches 2000 m of depth; few NE–SW hills, valleys and escarpments oriented have been identified West and East of the axis of the NWLSC and of the NLSC. In the Southern part, the NWLSC is offset by the Lau Extensional Transform Fault. The transition between the NWLSC and the NLSC is not clear, due to a scarcity of high-resolution bathymetry.

The morphology shows an alternation of NNE–SSW oriented hills and valley that in the Northern part are offset by a left-slip fracture zone, which we here call the North Lau Transform Fault. Along the NWLSC, we calculated a full spreading rate of 60.2 mm/year (Figure 5b); magnetic anomalies show a strong asymmetry of spreading rate.

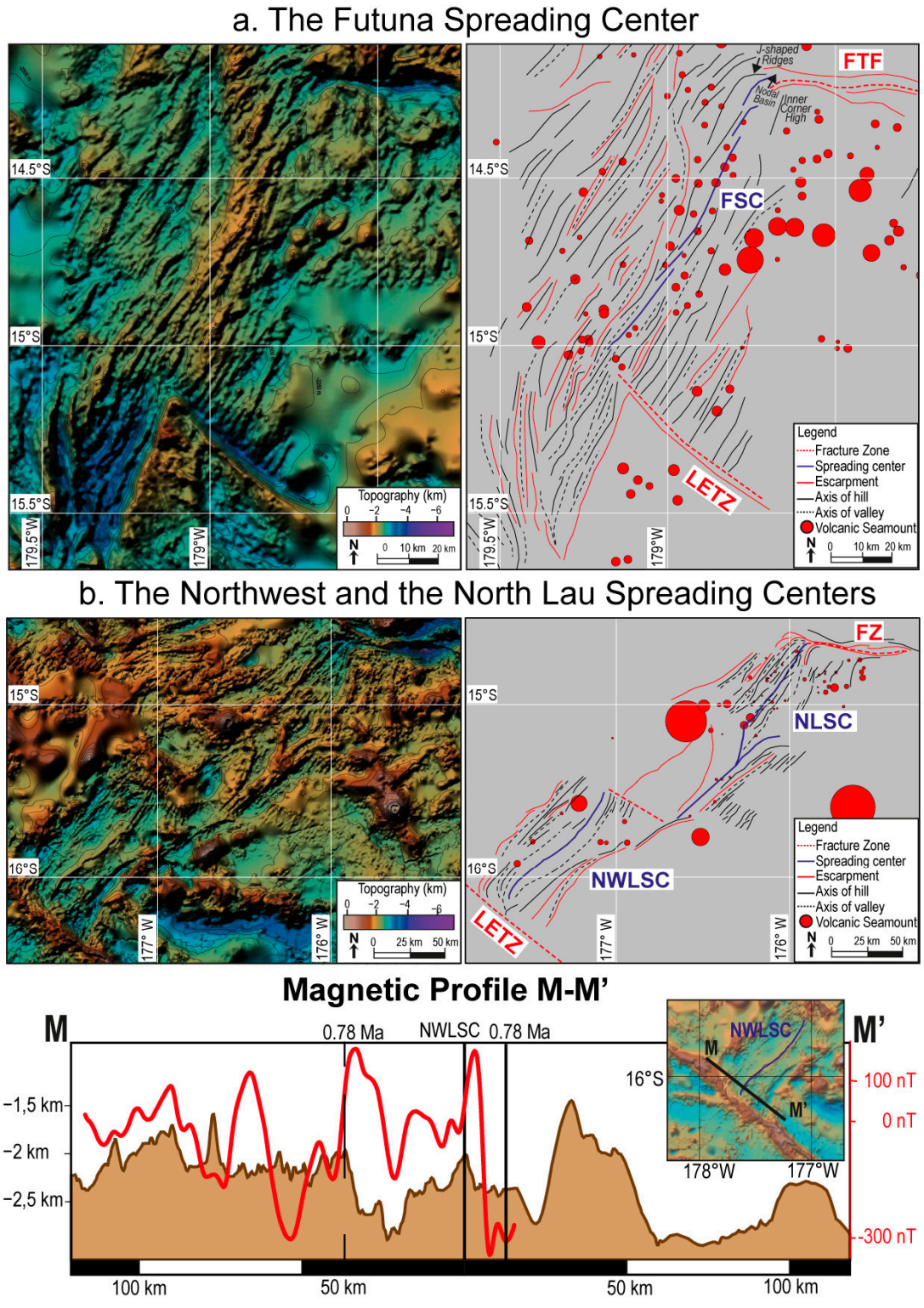

Figure 5. *Cont.*

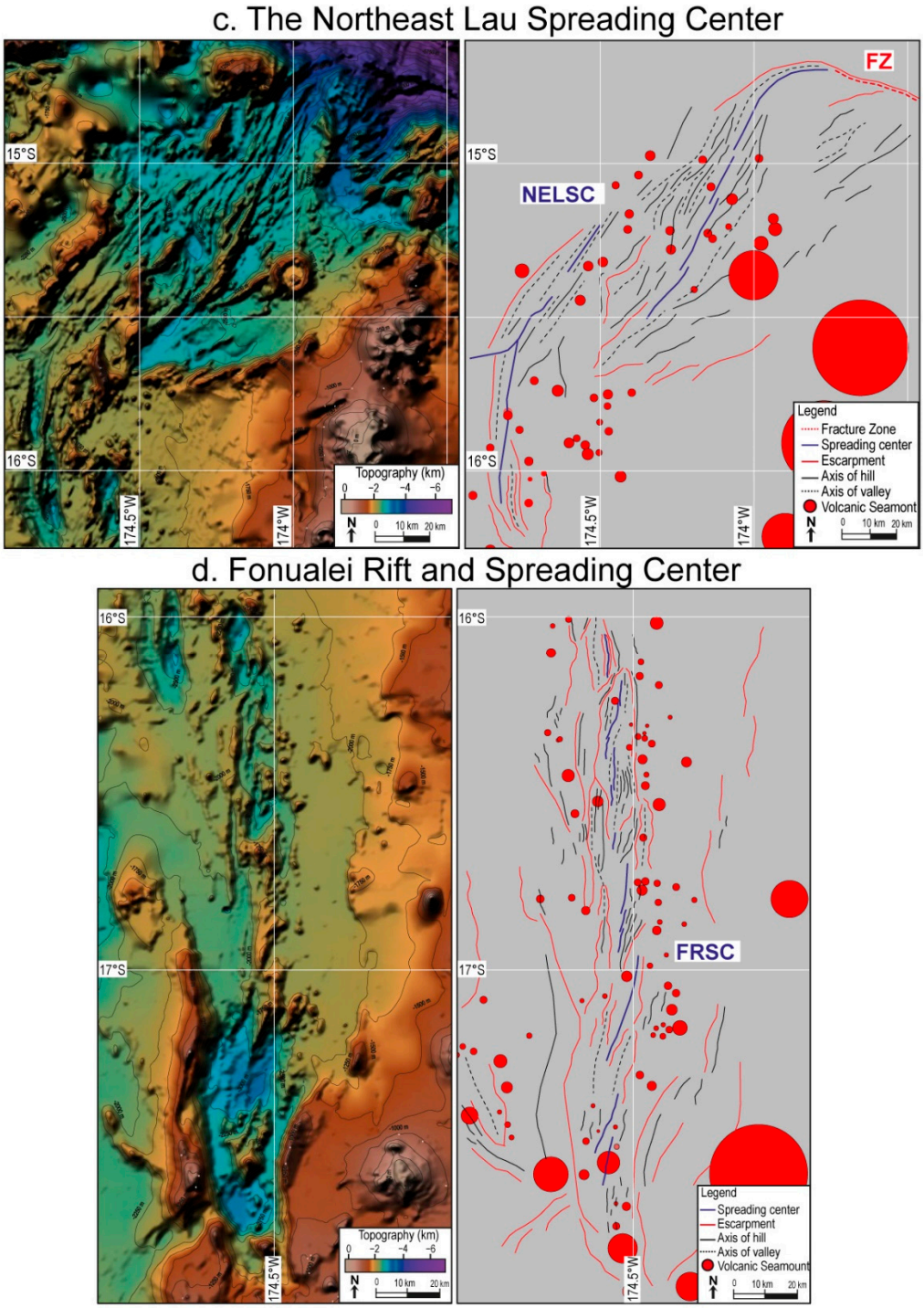

Figure 5. (**a**) Shaded relief image and regional morphological analysis of the Futuna Spreading Center region. (**b**) Shaded relief image and regional morphological analysis of the Northwest and North Lau Spreading Center region. Bathymetric and magnetic profile M–M′ crossing the Northwest Lau Spreading Center. FSC: Futuna Spreading Center; FTF: Futuna Transform Fault; NWLSC: Northwest Lau Spreading Center; NLSC: North Lau Spreading Center; LETZ: Lau Extensional Transform Zone; FZ: Fracture Zone. (**c**) Shaded relief image and regional morphological analysis of the Northeast Lau Spreading Center region. (**d**) Shaded relief image and regional morphological analysis of the Fonualei Rift and Spreading Center region. NELSC: Northeast Lau Spreading Center; FRSC: Fonualei Rift and Spreading Center; FZ: Fracture Zone.

The NELSC and the FRSC are located in the eastern part of the Lau Basin, ~200 km from the TSZ (Figures 1 and 5c,d). The NELSC is composed of two segments of back-arc spreading centers, both NNE–SSW oriented. The bathymetry along the FRSC region ranges from few meters above sea level to a maximum of 3208 m below sea level. The Northern part of the FRSC is composed of several N–S spreading segments and escarpments, ranging from −2250 to −1250 m. The southern part of the FRSC is characterized by a deep triangular valley (>−3000) bounded by left and right escarpments >15° steep. The maximum width of the valley reaches ~40 km. Several NNE–SSW hills are located in the valley. The area shows an intense magmatic activity represented by several volcanic seamounts of different size.

3.2. Numerical Models

The temperature structure (Figure 6A,C) predicted by the numerical model in the subduction trench area (~150 km wide, Figure 6C), points to a high temperature within a narrow thinned area, which is ~50 km wide, where the 300 °C and the 600 °C isotherms deepen, after reaching a slightly higher peak in temperature. In fact, right after the trench (~1350 km on the horizontal scale of the numerical domain), a 50 km wide area where the 900 °C isotherm approaches the surfaces can be seen. Then, the isotherms deepen until 150 km away from the trench (~1250 km on the horizontal numerical domain), where the 600 °C isotherm reaches approximately 25 km depth, pointing to another peak in temperature. This is better observable in Figure 6C, where a zoom on the trench area subject to these variations is shown. Together with these variations in the 300 °C, 600 °C, and 900 °C isotherms, as well as the 1200 °C, approaching the trench, they rise towards the 900 °C, contributing to form an area where the isotherms are closer than anywhere else in the numerical domain.

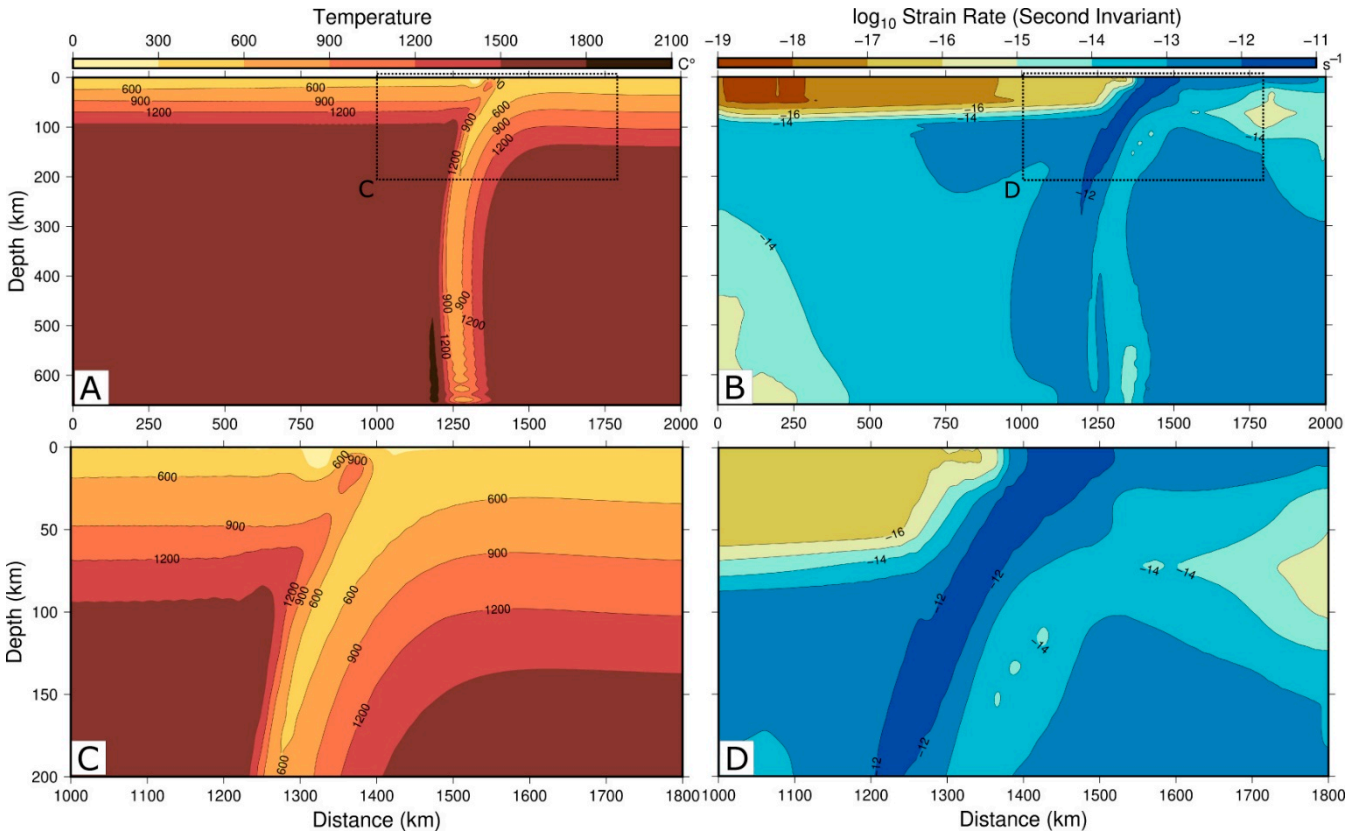

Figure 6. Numerical model results. This figure shows the temperature and the second invariant of the strain rate (**A**,**B**) of the numerical model results. The dotted squared points to areas shown in panels C and D. At ~1350 km, a 50 km wide area can be seen, where the 900 °C approaches the surfaces and the isotherms then deepen. The 600 °C isotherm then rises towards approximately 25 km depth,

150 km away from the trench (~1250 km), pointing to another peak in temperature. In addition, the 1200 °C, approaching the trench, rises towards the 900 °C (**C**), contributing to form an area where the isotherms are closer than anywhere else in the numerical domain. The second invariant of the strain rate (**B**,**D**) show higher deformation close to the subducting slab. However, an area of highly deforming material (10^{13} s^{-1}) extends ~750–800 km away from the trench, below the upper plate (**B**) and behind the slab. The deformation increases towards the trench, going from 10^{18} s^{-1} to ~10^{16} s^{-1} (**D**).

The second invariant of the strain rate (Figure 6B,D) show higher deformation close to the subducting slab. However, an area of highly deforming material (10^{13} s^{-1}) extends ~750–800 km away from the trench, below the upper plate (Figure 6B) and behind the slab. The deformation increases within the upper plate, towards the trench, going from 10^{18} s^{-1} in the undeformed part of the upper plate lithosphere, to ~10^{16} s^{-1} in the 250 km wide area right left of the trench, where the deformation within the upper plate lithosphere is concentrated (zoomed area of Figure 6D).

4. Discussion

A new oceanic crust in the Lau BAB South of the LETZ (Figure 1) forms along a system of BASCs where the spreading rate decreases southward from ~95 mm/year to 40 mm/year [22]; otherwise, North of the LETZ, an oceanic crust occurs along parallel spreading segments in a basin about 800 km wide (Figures 1 and 2). Here, the curved geometry and the superfast velocity of the Tonga subduction [31,74] cause a diffuse deformation on the overriding plate, with formation of spreading segments, transform faults/fracture zones, and triple junctions (i.e., the Mangatolu Triple Junction in Figure 1; 30). Those plate boundaries form different microplates, i.e., the Futuna, Niuafo'ou, and Tonga microplates [30,41]; unfortunately, their geometry and their evolution are very difficult to determine.

We did a morphological analysis of all spreading segments of the Northern Lau Basin. The FSC, NWLSC, NLSC, and NELSC resemble fast/intermediate MORs, showing smooth morphological rises; they generally lack a median valley, having instead an axial high some 1–2 km wide [75,76]. Intense volcanism, testified by several volcanic seamounts (Figures 5 and 7), characterized the flanks of those ridge segments. Morpho-lineaments have been clustered and plotted in rose diagrams to compare their trend (Figure 7): the FSC, the NLSC, the NWLSC, and the NELSC, all a NE–SW trend (~N40°E; green, yellow, and blue diagrams, respectively).

Furthermore, they are all offset by left-slip fracture zones in their relative northern part (black boxes in Figure 7): the FSC–FTF intersection in the western part of the Lau BAB; the NLSC–FZ intersection in the central part of the Lau BAB; and the NELSC–FZ intersection in the eastern part of the Lau BAB. These ridge-transform intersections show deep nodal basins, inner corner highs, and J-shaped ridges along the outside corner [77], resembling the morphology of slow ridge-transform intersections [50]. Along the FSC, this change of morphology reflects the decrease of spreading rate from 40 mm/year along the central summit of the FSC to 10 mm/year near the FSC–FTF intersection [44]. In the central and eastern part of the Northern Lau BAB, the spreading rates increase Northward: from 75 mm/year along the NWLSC to 110 mm/year along the NLSC [78] (and reference therein), and from 45 to 27 mm/year along the NELSC [39]. Most of those values are based on GPS measurements; here we improve the spreading rates data in the Northern Lau BAB, calculating a value of 60.2 mm/year along the NWLSC for the last 0.78 Ma (Figures 5b and 7) based on magnetic data.

The bathymetric rise and the lack of a median valley along the NWLSC is in line with the morphology of an intermediate/fast MOR [11–13]. Furthermore, magnetic profile M-M′ (Figure 5b) shows a strong spreading asymmetry for the last 0.78 Ma, in line with the magnetic data of [30].

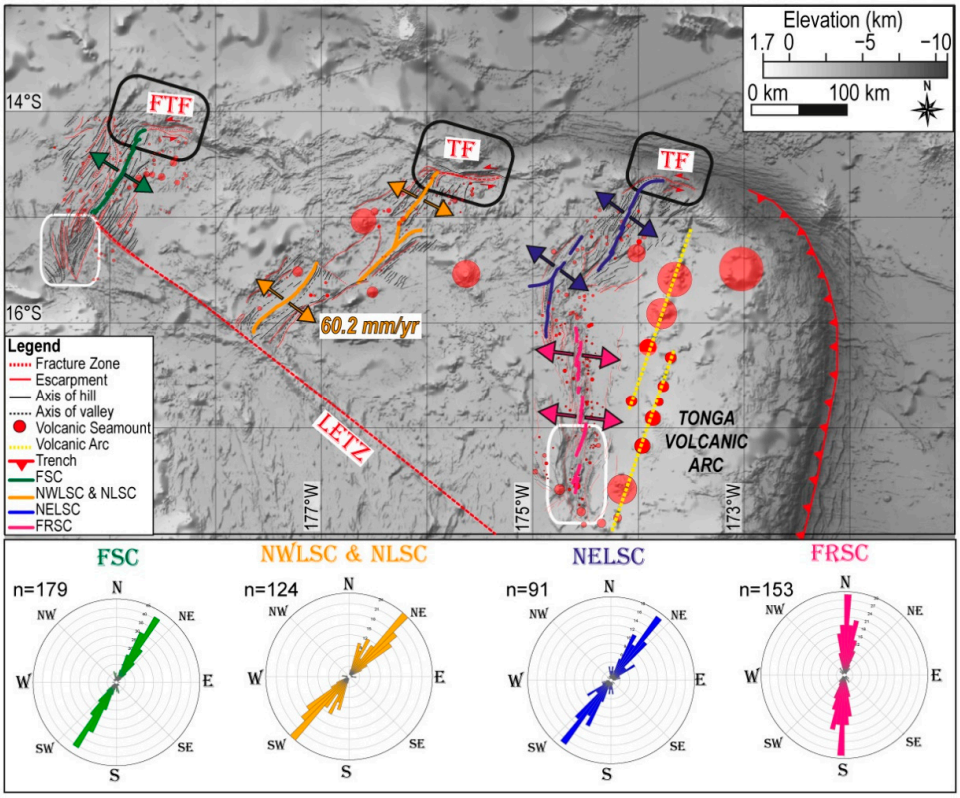

Figure 7. Shaded relief image of the Northern Lau Basin and main directions of the back-arc spreading centers; the arrows indicate the oblique direction of the spreading centers. Values of spreading centers along NWLSC based on the magnetic profile M–M′ are shown in Figure 5b; rose diagrams of the morpho-lineaments detected along the FSC, the NWLSC and NLSC, the NELSC and the FRSC. n: number of morpho-lineaments.

The FRSC, located in the eastern part of the basin, ~200 km West of the Tonga SZ, shows a N–S trend (~N5°E; pink diagram in Figure 7); this trend is parallel to the modern direction of the Tonga SZ. Together with our thermal model, showing a rise of the mantle about ~50 km West from the TSZ (Figure 7), this trend confirms that the mantle rise is now located below the Tonga volcanic arc and near the FRSC. The full spreading rates along the FRSC decrease Southward: from 27 mm/year to only 8 mm/year. This can be considered a rift propagating southward [39,41]. According to [44], the Southern part of the FSC could also be a propagating rift. Comparing the Southern parts of the FSC and the FRSC (white boxes in Figure 7), we note that: (a) the trend of their morpho-lineaments is mainly N–S; (b) the range of bathymetry (from −2500 to −3500 m) is similar and differs from the shallow bathymetry of the other Northern Lau BASc; c) they both show a triangular shape propagating Southward. We note also some differences: (a) there is a lack of volcanism along the FSC, whereas along the FRSC we identified several volcanic seamounts; (b) the focal mechanisms along the FSC are mainly strike-slip, whereas along the FRSC we observe normal faults; (c) the morphology of the FSC, consisting of an alternation of several curved hills and valleys, is most complicated with respect to that of the FRSC, where two main escarpments, one on the left, and one on the right, delimit a triangular valley with inside N–S elongated seamounts. We assume that, because the modern deformation in the Northern Lau Basin is located North of the LETZ (Figure 7), the formation of oceanic crust along the Southern part of the FSC is no longer active, but is affected by strike-slip tectonics (Figure 2a) along older tectonic lineaments, as shown also by [38] for some area of the Northern Lau Basin.

We created two conceptual models where we correlate the bathymetry of the Northern Lau Basin with the distribution of the temperature and of the second invariant of the strain

rate in the mantle (Figure 8). Models dissect the region, as shown in Figure 2: they are oriented NE–SW and cross, from West to East, to two mature spreading segments (FSC and NWLSC) and the younger FRSC. We marked in our models with a black line the bathymetric profile, with a red dashed line the crustal thickness, and with white arrows the location of the spreading segments. The peak of temperature ~50 km west of the TSZ (Figure 8a) shows that the rise of the mantle is now located in a narrow area below the Tonga volcanic arc (Figure 7) and the FRSC (Figure 8a). The deformation pattern observed in the simulation of the retreating Superfast TSZ (Figure 8b) evidences an area were the log 10 of the second invariant of the strain rate is higher than anywhere else in front of the Pacific slab, i.e., from the Tonga subduction to ~800 km westward within more than 200 km depth in the mantle, including the area where the NWLSC and the FSC are still active. Based on their similar trend, on their "mature" morphology, and on the repetition of their ridge-transform northern intersections, the FSC, NWLSC, NLSC, and NELSC show the inheritance of the tectonic deformation left from the superfast TSZ on the overriding plate during the last Ma. Our results show that the occurrence of oceanic crust along those spreading centers is due to a wide mantle deformation in the study domain, which induces mantle circulation, feeding them in the same back-arc basin.

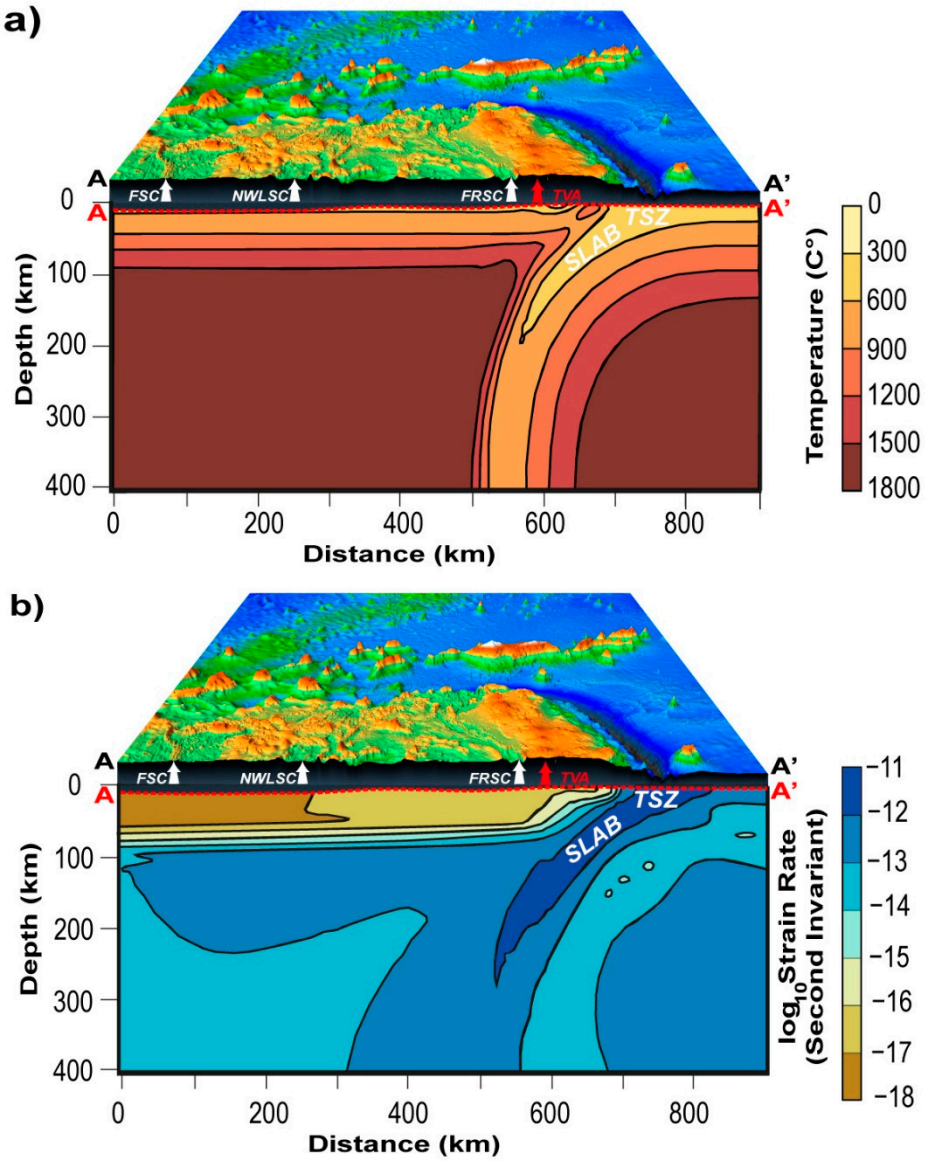

Figure 8. Conceptual models showing the regional bathymetry of the Northern Lau Basin: (**a**) the

distribution of the temperature in the mantle; (**b**) the second invariant of the strain rate, both predicted by our numerical model. The 3D bathymetry was created using the open source software 3DEM (visualization software created by Richard Horne, USGS, http://www.hangsim.com/3dem/, accessed on 1 July 2021). Black line A–A': bathymetric profile shown in Figure 2c. Red dashed line A-A': crustal thickens shown in Figure 2c. White arrows indicate the location of the mantle rise below the back arc spreading centers. FSC: Futuna Spreading Center; NWLSC: Northwest Lau Spreading Center; FRSC: Fonualei Rift and Spreading Center; TSZ: Tonga Subduction Zone; TVA: Tonga Volcanic Arc.

5. Conclusions

The TSZ is located in a complex area, where several processes took place in the past (and still do). The Northern part of the Lau Basin is a region where the modern deformation due to extensional tectonics creates episodes from back-arc rifting to back-arc spreading. We analyzed the morphology of all the segments of back-arc spreading centers located in the Northern Lau Basin, showing two major trends: the FSC, NLSC, NWLSC, and NELSC are NE–SW oriented; the FRSC is N–S oriented. We improved the spreading rate data of the Northern Lau Basin, calculating a full spreading rate of 60.2 mm/year along the NWLSC. Furthermore, we created 2D numerical models including visco-plastic rheologies and prescribed surface velocities in an upper plate-fixed reference frame. A step further in reproducing tectonics of this area could be the realization of a 3D numerical model in which complex geometries could interact at longer time-spans. Our models show an area of active deformation from the Tonga Superfast Subduction trench to ~800 km westward within the mantle, which matches the formation of the Fonualei Rift and Spreading Center and potentially contributes to the volcanic centers in the Northern Lau Basin.

Author Contributions: Conceptualization, C.P. and M.C.; methodology, C.P., E.F., M.F.L. and F.M.; software, C.P., E.F., M.F.L., M.C. and F.M.; formal analysis, C.P.; data curation, C.P.; writing—original draft preparation, C.P.; writing—review and editing, C.P., E.F., M.F.L., M.C. and F.M. All authors have read and agreed to the published version of the manuscript.

Funding: This research received no external funding.

Data Availability Statement: Bathymetric data are available from the database GEBCO 2020 Bathymetry. Magnetic data are from the NGDC database. Earthquake data are available in a publicly accessible database (https://www.emsc-csem.org/Earthquake/, accessed on 1 March 2021). Seismic data presented in this study are available on request.

Acknowledgments: We thank the Computational Infrastructure for Geodynamics (geodynamics.org), which is funded by the National Science Foundation under award EAR-0949446 and EAR-1550901 for supporting the development of ASPECT. Comments by the reviewer Christian Vérard and by two other anonymous reviewers were useful to improve the manuscript. Many thanks are due to E. Bonatti (LDEO-Columbia University; Ismar-CNR) for his advice. Work supported by the ISMAR (CNR)-ISPRA partnership. Economic funds from EMODnet Geology 3 project.

Conflicts of Interest: The authors declare no conflict of interest.

References

1. Crameri, F.; Conrad, C.P.; Montési, L.; Lithfow-Bertelloni, C.R. The dynamic life of an oceanic plate. *Tectonophysics* **2019**, *760*, 107–135. [CrossRef]
2. Vine, F.J.; Matthews, D.H. Magnetic Anomalies over Oceanic Ridges. *Nature* **1963**, *199*, 949. [CrossRef]
3. Parson, B.; Sclater, J.G. An analysis of the variation of ocean floor bathymetry and heat flow with age. *J. Geophys. Res.* **1977**, *82*, 803–827. [CrossRef]
4. Hynes, A.; Mott, J. On the causes of back-arc spreading. *Geology* **1985**, *13*, 387–389. [CrossRef]
5. Uyeda, S.; Kanamori, H. Back-arc opening and the mode of subduction. *J. Geophys. Res.* **1979**, *84*, 1049–1061. [CrossRef]
6. Doglioni, C.; Gueguen, E.; Harabaglia, P.; Mongelli, F. On the origin of west-directed subduction zones and applications to the western Mediterranean. *Geol. Soc. Lond. Spec. Publ.* **1999**, *156*, 541–561. [CrossRef]
7. Leat, P.T.; Larter, R.D. Intra-oceanic subduction systems: Introduction. *Geol. Soc. Lond. Spec. Publ.* **2003**, *219*, 1–17. [CrossRef]
8. Sdrolias, M.; Muller, R.D. Controls on back-arc basin formation. *Geochem. Geophys. Geosyst.* **2006**, *7*, 1–40. [CrossRef]

9. Greve, S.; Paulssen, H.; Goes, S.; Van Bergen, M. Shear-velocity structure of the Tyrrhenian Sea: Tectonics, volcanism and mantle (de) hydration of a back-arc basin. *Earth Planet. Sci. Lett.* **2014**, *400*, 45–53. [CrossRef]
10. Marcuson, R.; Blackman, D.K.; Harmon, N. Seismic anisotropy predicted for 2-D plate-driven flow in the Lau back—Arc basin. *Phys. Earth Planet. Int.* **2014**, *233*, 88–94. [CrossRef]
11. Perfit, M.R.; Chadwick, W.W. Magmatism at mid-ocean ridges: Constraints from volcanological and geochemical investigations. *Geophys. Monogr.-Am. Geophys. Union* **1998**, *106*, 59–116.
12. Small, C. *Faulting and Magmatism at Mid-Ocean Ridges*; Buck, W., Delaney, P.T., Karson, J.A., Lagabrielle, Y., Eds.; American Geophysical Union: Washington, DC, USA, 1998; pp. 1–26.
13. Dick, H.J.B.; Lin, L.; Schouten, H. An ultraslow-spreading class of ocean ridge. *Nature* **2003**, *426*, 405–412. [CrossRef]
14. Magni, V. The effects of back-arc spreading on arc magmatism. *Earth Planet. Sci. Lett.* **2019**, *519*, 141–151. [CrossRef]
15. Van der Broek, J.M.; Magni, V.; Gaina, C.; Biuter, S.J.H. The Formation of Continental Fragments in Subduction Settings: The Importance of Structural Inheritance and Subduction System Dynamics. *J. Geophys. Res. Solid Earth* **2019**, *125*, e2019JB018370.
16. Zellmer, K.E.; Taylor, B. A three-plate kinematic model for the Lau Basin Opening. *Geochem. Geophys. Geosyst.* **2003**, *2*, 2000GC000106. [CrossRef]
17. Karig, D.E.; Anderson, R.N.; Bibee, L.T. Characteristics of back arc spreading in the Mariana Trough. *J. Geophys. Res. Solid Earth* **1978**, *83*, 1213–1226. [CrossRef]
18. Weissel, J.K. Magnetic lineations in marginal basins of the western Pacific. *Philos. Trans. R. Soc. Lond. Ser. A Math. Phys. Sci.* **1981**, *300*, 223–247.
19. Parson, L.M.; Hawkins, J.W. Two-stage ridge propagation and the geological history of the Lau backarc basin. *Proc. Ocean Drill. Program Sci. Results* **1994**, *135*, 819–828.
20. Heezen, B.C.; Johnson, G.L. The South Sandwich Trench. *Deep-Sea Res.* **1965**, *12*, 185–197. [CrossRef]
21. Livermore, R.; Cunningham, A.; Vanneste, L.; Larter, R. Subduction influence on magma supply at the East Scotia Ridge. *Earth Planet. Sci. Lett.* **1997**, *150*, 261–275. [CrossRef]
22. Karig, D.E. Ridges and Basins of the Tonga-Kermadec Island Arc System. *J. Geophys. Res.* **1970**, *75*, 239–254. [CrossRef]
23. Martinez, F.; Taylor, B. Mantle wedge control on back-arc crustal accretion. *Nature* **2002**, *416*, 417–420. [CrossRef]
24. Weissel, J.K.; Hayes, D.E.; Herron, E.M. Plate tectonics synthesis: The displacements between Australia, New Zealand, and Antarctica since the Late Cretaceous. *Mar. Geol.* **1977**, *25*, 231–277. [CrossRef]
25. Malahoff, A.; Feden, R.H.; Fleming, H.S. Magnetic anomalies and tectonic fabric of marginal basins north of New Zealand. *J. Geophys. Res.* **1982**, *87*, 4109–4125. [CrossRef]
26. Taylor, B.; Zellmer, K.; Martinez, F.; Goodlie, A. Seafloor spreading in the Lau back-arc basin. *Earth Planet. Sci. Lett.* **1996**, *144*, 35–40. [CrossRef]
27. Parson, L.M.; Wright, I.C. The Lau-Havre-Taupo back-arc basin: A southward-propagating, milti-stage evolution from rifting to spreading. *Tectonophysics* **1996**, *263*, 1–22. [CrossRef]
28. Fujiwara, T.; Yamazaki, T.; Joshima, M. Bathymetry and magnetic anomalies in the Havre Trough and southern Lau Basin: From rifting to spreading in back-arc basins. *Earth Planet. Sci. Rev.* **2001**, *185*, 253–264. [CrossRef]
29. Ruellan, E.; Delteil, J.; Wright, I.; Matsumoto, T. From rifting to active spreading in the Lau Basin—Havre Trough backarc system (SW Pacific)—Locking/unlocking induced by seamount chain subduction. *Geochem. Geophys. Geosyst.* **2006**, *4*. [CrossRef]
30. Caratori Tontini, F.; Bassett, D.; De Ronde, C.E.J.; Timm, C.; Wysoczanski, R. Early evolution of a young back-arc basin in the Havre Trough. *Nat. Geosci.* **2019**, *12*, 856–862. [CrossRef]
31. Bevis, M.; Taylor, F.W.; Schutz, B.E.; Recy, J.; Isacks, B.L.; Helu, S.; Calmantli, S. Geodetic observations of very rapid convergence and back-arc extension at the Tonga arc. *Nature* **1995**, *374*, 249–251. [CrossRef]
32. Dziewonski, A.M.; Chou, T.A.; Woodhouse, J.H. Determination of earthquake source parameters from waveform data for studies of global and regional seismicity. *J. Geophys. Res.* **1981**, *86*, 2825–2852. [CrossRef]
33. Ekstrom, G.; Nettles, M.; Dziewonski, A.M. The global CMT project 2004-2010: Centroid moment tensors for 13,017 earthquakes. *Phys. Earth Planet. Int.* **2012**, *200*, 1–9. [CrossRef]
34. Wessel, P.; Smith, W.H.; Scharroo, R.; Luis, J.; Wobbe, F. Generic mapping tools: Improved version released. *Eos Trans. Am. Geophys. Union* **2013**, *94*, 409–410. [CrossRef]
35. Crameri, F.; Shepard, G.E.; Heron, P.J. The misuse of colour in science communication. *Nat. Commun.* **2020**, *11*, 5444. [CrossRef]
36. De Mets, C.; Gordon, R.G.; Argus, D.F. Geologically current plate motions. *Geophys. J. Int.* **2010**, *181*, 1–80. [CrossRef]
37. Müller, R.D.; Zahirovic, S.; Williams, S.E.; Cannon, J.; Seton, M.; Bower, D.J.; Tetley, M.G.; Heine, C.; Le Breton, E.; Liu, S.; et al. A global plate model including lithospheric deformation along major rifts and orogens since the Triassic. *Tectonics* **2019**, *38*, 1884–1907. [CrossRef]
38. Baxter, A.T.; Hannington, M.D.; Stewart, M.S.; Emberley, J.M.; Brejer, K.; Kratschell, A.; Petersen, S.; Brandl, P.A.; Klischies, M.; Mensing, R.; et al. Shallow Seismicity and the Classification of Structures in the Lau Back-Arc Basin. *Geochem. Geophys. Geosyst.* **2020**, *21*, e2020GC008924. [CrossRef]
39. Baker, E.T.; Sharon, L.W.; Massoth, G.J.; Resing, J.A. The NE Lau Nasin: Widespread and Abundant Hydrothermal Venting in Back-Arc Region behind a Superfast Subduction Zone. *Front. Mar. Sci.* **2019**, *6*, 382. [CrossRef]
40. Segev, A.; Rybakov, M.; Mortimer, N. A crustal model for Zoelandia and Fiji. *Geophys. J. Int.* **2012**, *189*, 1277–1292. [CrossRef]

41. Sleeper, J.D.; Martinez, F.; Arculus, R. The Fonualei rift and spreading Center: Effects of ultraslow spreading and arc proximity on back-arc crustal accretion. *J. Geophys. Res. Solid Earth* **2016**, *121*, 4814–4835. [CrossRef]
42. Van de Lagemaat, S.H.A.; Van Hinsbergen, D.J.J.; Boschman, L.M.; Kamp, P.J.J.; Spakman, W. Southwest Pacific absolute plate kinematic reconstruction reveals major Cenozoic Tonga-Kermadec slab dragging. *Tectonics* **2018**, *37*, 2647–2674. [CrossRef]
43. Seton, M.; Müller, R.D.; Zahirovic, S.; Gaina, C.; Torsvik, T.; Shephard, G. Global continental and ocean basin reconstructions since 200 Ma. *Earth-Sci. Rev.* **2012**, *113*, 212–270. [CrossRef]
44. Garel, E.; Lagabrielle, Y.; Pelletier, B. Abrupt axial variations along the slow to ultra-slow spreading centers of the northern North Fiji Basin (SW Pacific): Evidence for short wave heterogeneities in a back-arc mantle. *Mar. Geophys. Res.* **2003**, *24*, 245–263. [CrossRef]
45. Szitkar, F.; Dyment, J.; Fouquet, Y. Widespread volcanism Southeast of Futuna Island (SW Pacific Ocean): Near-seafloor magnetic dating and regional consequences. *J. Volcanol. Geotherm. Res.* **2020**, *406*, 107064. [CrossRef]
46. Lytle, M.L.; Kelley, K.A.; Hauri, E.H.; Gill, J.B.; Papia, D.; Arculus, R.J. Tracing mantle sources and Samoan influence in the northwestern Lau back-arc basin. *Geochem. Geophys. Geosyst.* **2012**, *13*, Q10019. [CrossRef]
47. Anderson, M.O.; Norris-Julseth, C.; Rubin, K.H.; Haase, K.; Hannington, M.D.; Baxter, A.T.; Stewart, M.S. Geologic and Structural Evolution of the NE Lau Basin, Tonga: Morphotectonic Analysis and Classification of Structures Using Shallow Seismicity. Front. *Front. Earth Sci.* **2021**, *9*, 665185. [CrossRef]
48. Wilson, J.Y. A new class of faults and their bearing on continental drifts. *Nature* **1965**, *207*, 343–347. [CrossRef]
49. Sykes, L.R. Mechanism of earthquakes and nature of faulting on the Mid-Atlantic Ridge. *J. Geoph. Res.* **1967**, *72*, 2131–2153. [CrossRef]
50. Fox, J.P.; Gallo, G. A tectonic model for Ridge-Transform–Ridge plate boundaries: Implications for the structure of oceanic lithosphere. *Tectonophysics* **1984**, *104*, 205–242. [CrossRef]
51. Smith, D.K.; Cann, J.R. Building the crust at the Mid-Atlantic Ridge. *Nature* **1993**, *365*, 707–715. [CrossRef]
52. Escartin, J.; Cannat, M. Ultramafic exposures and the gravity signature of the lithosphere near the Fifteen-Twenty Fracture Zone (Mid-Atlantic Ridge, 14°–16.5°N). *Earth Planet. Sci. Lett.* **1999**, *171*, 411–424. [CrossRef]
53. Rundquist, D.V.; Sobolev, P.O. Seismicity of mid-oceanic ridges and its geodynamic implications: A review. *Earth-Sci. Rev.* **2002**, *58*, 143–161. [CrossRef]
54. Smith, D.K.; Escartín, J.; Cannat, M.; Tolstoy, M.; Fox, C.G.; Bohnenstiehl, D.R.; Bazin, R. Spatial and temporal distribution of seismicity along the northern Mid-Atlantic Ridge (15°–35°N). *J. Geoph. Res.* **2003**, *108*, 8-1–8-22. [CrossRef]
55. Harris, P.T.; Macmillian-Lawler, M.; Rupp, J.; Baker, E.K. Geomorphology of the oceans. *Mar. Geol.* **2014**, *352*, 4–24. [CrossRef]
56. National Geophysical Data Center (NOAA). Marine Trackline Geophysical Database. 1977. Available online: https://www.ncei.noaa.gov/access/metadata/landing-page/bin/iso?id=gov.noaa.ngdc:G00129 (accessed on 12 December 2021).
57. Thébault, E.; Finlay, C.C.; Beggan, C.D. International Geomagnetic Reference Field: The 12th generation. *Earth Planet. Sp.* **2015**, *67*, 79.
58. Mendel, V.; Munschy, M.; Sauter, D. MODMAG, a MATLAB program to model marine magnetic anomalies. *Comp. Geosci.* **2005**, *31*, 589–597. [CrossRef]
59. Cande, S.C.; Kent, D.V. Revised calibration of the geomagnetic polarity time scale for the Late Cretaceous and Cenozoic. *J. Geophys. Res.* **1995**, *100*, 6093–6095. [CrossRef]
60. Kronbichler, M.; Heister, T.; Bangerth, W. High Accuracy Mantle Convection Simulation through Modern Numerical Methods. *Geophys. J. Int.* **2012**, *191*, 12–29. [CrossRef]
61. Heister, T.; Dannberg, J.; Gassmöller, R.; Bangerth, W. High Accuracy Mantle Convection Simulation through Modern Numerical Methods—II: Realistic Models and Problems. *Geophys. J. Int.* **2017**, *210*, 833–851. [CrossRef]
62. Bangerth, W.; Dannberg, J.; Gassmoeller, R.; Heister, T. ASPECT v2.2.0. (Version v2.2.0). Zenodo. 2020. Available online: https://zenodo.org/record/3924604#.YegJmvgRVPY (accessed on 12 December 2021).
63. Schubert, G.; Turcotte, D.L.; Olson, P. *Mantle Convection in the Earth and Planets*; Part 1; Cambridge University Press: Cambridge, UK, 2001.
64. Glerum, A.; Thieulot, C.; Frater, M.; Blom, C.; Spakman, W. Nonlinear viscoplasticity in ASPECT: Benchmarking and applications to subduction. *Solid Earth* **2018**, *9*, 267–294. [CrossRef]
65. Gerya, T. *Introduction to Numerical Geodynamic Modelling*; Cambridge University Press: Cambridge, UK, 2010.
66. Ficini, E.; Cuffaro, M.; Doglioni, C. Asymmetric dynamics at subduction zones derived from plate kinematic constraints. *Gondwana Res.* **2020**, *78*, 110–125. [CrossRef]
67. Doglioni, C.; Carminati, E.; Cuffaro, M.; Scrocca, D. Subduction kinematics and dynamic constraints. *Earth Sci. Rev.* **2007**, *83*, 125–175. [CrossRef]
68. Müller, R.D.; Sdrolias, M.; Gaina, C.; Roest, W.R. Age, spreading rates, and spreading asymmetry of the world's ocean crust. *Geochem. Geophys. Geosyst.* **2008**, *9*, Q04006. [CrossRef]
69. Müller, R.D.; Seton, M.; Zahirovic, S.; Williams, S.E.; Matthews, K.J.; Wright, N.M.; Shephard, G.E.; Maloney, K.T.; Barnett-Moore, N.; Hosseinpour, M.; et al. Ocean basin evolution and global-scale plate reorganization events since Pangea breakup. *Ann. Rev. Earth Planet. Sci.* **2016**, *44*, 107–138. [CrossRef]
70. Vérard, C.; Stamfli, G.M. Geodynamic reconstructions of the Australides-2: Mesozoic-Cainozoic. *Geosciences* **2013**, *3*, 331–353. [CrossRef]

71. Ribeiro, J.M.; Stern, R.J.; Martinez, F.; Woodhead, J.; Chen, M.; Ohara, Y. Asthenospheric outflow from the shrinking Philippine Sea Plate: Evidence from HfeNd isotopes of southern Mariana lavas. *Earth Planet. Sci. Lett.* **2017**, *478*, 258–271. [CrossRef]
72. Ranalli, G. *Rheology of the Earth*, 2nd ed.; Chapman Hall: London, UK, 1995.
73. Clauser, C.; Huenges, E. Thermal conductivity of rocks and minerals. In *Rock Physics and Phase Relations*; Ahrens, T.J., Ed.; Reference Shelf 3; AGU: Washington DC, USA, 1995; pp. 105–126.
74. Mallard, C.; Coltice, N.; Seton, M.; Müller, R.D.; Tackley, P.J. Subduction controls the distribution and fragmentation of Earth's tectonic plates. *Nature* **2016**, *535*, 140–143. [CrossRef]
75. Spiess, F.N.; Macdonald, K.C.; Atwater, T.; Ballard, R.; Carranza, A.; Cordoba, D.; Rangin, C. East Pacific Rise: Hot springs and geophysical experiments. *Science* **1980**, *207*, 1421–1433. [CrossRef]
76. Fornari, D.J.; Von Damm, K.L.; Bryce, J.G.; Cowen, J.P.; Ferrini, V.; Fundis, A.; Adams, D.K. The East Pacific Rise between 9 N and 10 N: Twenty-five years of integrated, multidisciplinary oceanic spreading center studies. *Oceanography* **2012**, *25*, 18–43. [CrossRef]
77. Grevemeyer, I.; Rüpke, L.H.; Morgan, J.P.; Iyer, K.; Devey, C.W. Extensional tectonics and two-stage crustal accretion at oceanic transform faults. *Nature* **2021**, *591*, 402–407. [CrossRef]
78. Lupton, J.; Rubin, K.H.; Arculus, R.; Lilley, M.; Butterfield, D.; Resing, J.; Baker, E.; Embley, R. Helium isotope, C/^{3}He, and Ba-Nb-Ti signatures in the northern Lau Basin: Distinguishing arc, back-arc, and hotspot affinities. *Geochem. Geophys. Geosyst.* **2020**, *16*, 1133–1155. [CrossRef]